

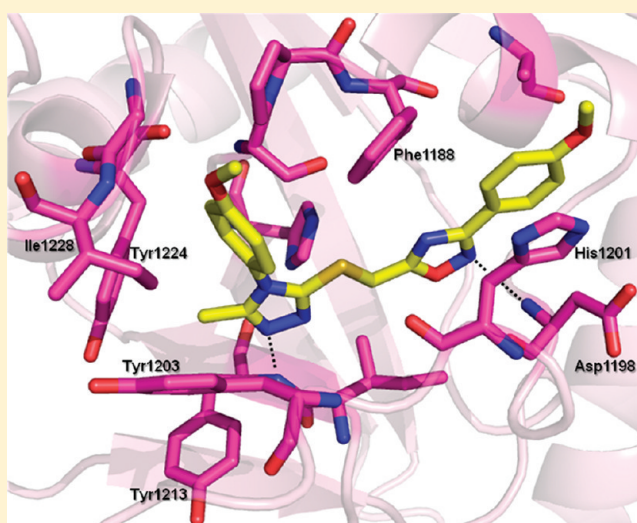
[1,2,4]Triazol-3-ylsulfanylmethyl)-3-phenyl-[1,2,4]oxadiazoles: Antagonists of the Wnt Pathway That Inhibit Tankyrases 1 and 2 via Novel Adenosine Pocket Binding

Michael D. Shultz,* Christina A. Kirby, Travis Stams, Donovan N. Chin, Jutta Blank, Olga Charlat, Hong Cheng,[†] Atwood Cheung, Feng Cong, Yun Feng, Pascal D. Fortin, Tami Hood, Viraj Tyagi, Ming Xu, Bailin Zhang,[†] and Wenlin Shao

Novartis Institutes for Biomedical Research, Inc., Cambridge, Massachusetts 02319, United States

Supporting Information

ABSTRACT: The Wnt signaling pathway is critical to the regulation of key cellular processes. When deregulated, it has been shown to play a crucial role in the growth and progression of multiple human cancers. The identification of small molecule modulators of Wnt signaling has proven challenging, largely due to the relative paucity of druggable nodes in this pathway. Several recent publications have identified small molecule inhibitors of the Wnt pathway, and tankyrase (TNKS) inhibition has been demonstrated to antagonize Wnt signaling via axin stabilization. Herein, we report the early hit assessment of a series of compounds previously reported to antagonize Wnt signaling. We report the biophysical, computational characterization, structure–activity relationship, and physicochemical properties of a novel series of [1,2,4]triazol-3-ylsulfanylmethyl)-3-phenyl-[1,2,4]oxadiazole inhibitors of TNKS1 and 2. Furthermore, a cocrystal structure of compound **24** complexed to TNKS1 demonstrates an alternate binding mode for PARP family member proteins that does not involve interactions with the nicotinamide binding pocket.



INTRODUCTION

Tankyrase (TNKS) proteins belong to the family of poly(ADP-ribose) polymerases (PARPs), which are enzymes utilizing NAD⁺ as a substrate to generate ADP-ribose polymers onto target proteins (PARsylation) (Figure 1).¹ There are two isoforms of TNKS, TNKS1 and TNKS2; both share overlapping functions and similar structures including the ankyrin (ANK) repeat domain, the sterile alpha molecule domain (SAM), and the catalytic PARP domain.² The ankyrin domain is important for mediating protein–protein interactions, and the SAM domain mediates mono- and heteromultimerization of TNKS. Multiple proteins with diverse biological functions have been discovered to associate with and are PARsylated by TNKS. Through binding and modulating these interacting proteins, TNKS plays a role in regulating a variety of cellular processes, including telomere elongation, sister telomere cohesion, mitotic spindle pole function, and membrane translocation of Golgi-associated vesicles upon insulin stimulation.^{2,3} More recently, TNKS has been shown to regulate the activity of the Wnt/ β -catenin pathway in colon cancer cells through PARsylation and destabilization of the Axin proteins.⁴

Dysregulation of Wnt signaling has been associated with multiple pathological states, including the development and progression of several types of cancer. Axin2 has been demonstrated to have a role in remyelination, and it was recently demonstrated that XAV939 (**1**), a TNKS inhibitor that stabilizes Axin2 levels, accelerated the differentiation and myelination of oligodendrocyte progenitor cells from brain and spinal cord after hypoxic and demyelinating injury.⁵

Pharmacological agents that attenuate Wnt signaling have been lacking for want of druggable nodes until very recently. Several groups have recently reported success in discovering small molecule inhibitors of the Wnt pathway (Figure 2) by employing high throughput screening that relies upon a readout of Wnt signaling.^{6–9} A key challenge with such an approach is the identification of the target protein or node that is modulated by the screening hits. We recently reported a chemical genetics approach whereby the PARP5a (TNKS1) and PARP5b (TNKS2) were identified as target proteins whose

Received: August 22, 2011

Published: January 19, 2012

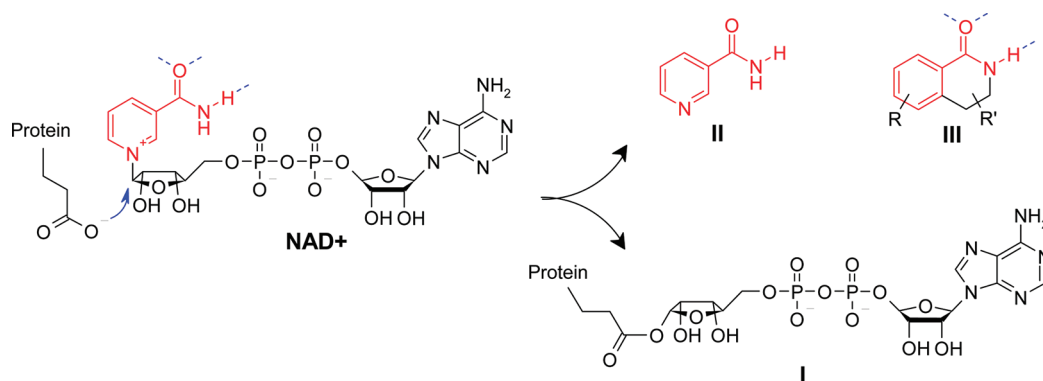


Figure 1. Post translational modification reaction catalyzed by poly ADP-ribose polymerase (PARP). The ADP-ribose moiety from NAD⁺ is transferred to a glutamic acid residue of the target protein to form I, releasing nicotinamide II. The key hydrogen bond interactions with the nicotinamide moiety help define a common pharmacophore of PARP inhibitors III.

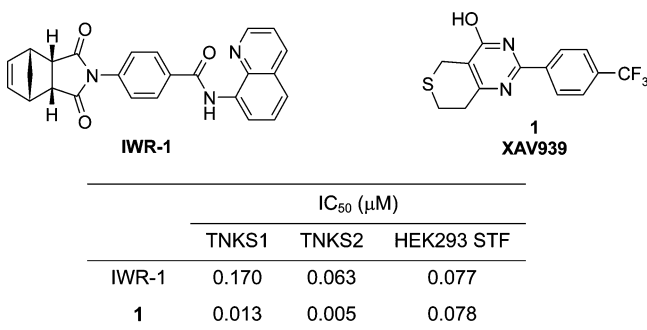


Figure 2. Previously reported small molecule modulators of Wnt signaling that act via TNKS inhibition.^{4,33}

enzymatic function was required for Wnt signaling.⁴ By employing a high throughput biochemical screen against TNKS2, additional chemical structures were identified that modulate Wnt signaling by direct inhibition of TNKS1 and TNKS2 enzymatic activity (Figure 2). For the biochemical assays in this manuscript, protein containing only the catalytic PARP domain of each TNKS isoform (also known as T-PARP) were used, and it has been previously shown the auto-PARsylation kinetics of full length and T-PARP TNKS are comparable.¹⁰

RESULTS AND DISCUSSION

Waalder et al. recently identified two small molecules, **2** (JW67) and **3** (JW74), as inhibitors of Wnt signaling (Figure 3) in the

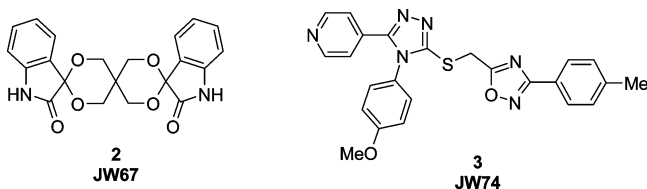


Figure 3. Small molecule modulators of Wnt signaling.

HEK293-STF assay, with IC₅₀s of 1.17 and 0.79 μM, respectively; however, the molecular target of inhibition was unknown or not disclosed.¹¹ These compounds, commercially available for high throughput screening (HTS) collections, were also identified in our HTS screen for TNKS inhibitors. As part of the screening cascade in our hit to lead activities with **3**, biochemical activity against TNKS1 and TNKS2 were

measured as well as cellular signaling in the HEK293-STF assay and a direct measurement of Axin2 stabilization in an Axin ELISA assay. Compound **3** inhibits TNKS1 and TNKS2 with IC₅₀s of 2.55 and 0.65 μM, respectively, and in excellent agreement with the values obtained by Waalder et al., an IC₅₀ of 0.548 μM was determined in our Wnt signaling HEK293-STF assay.

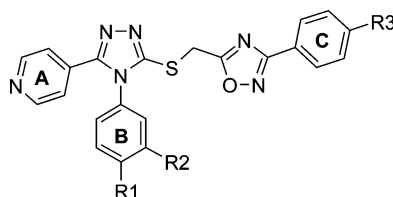
Our primary goal was to make a rapid assessment of the potential for this series to be optimized successfully and prioritize further efforts accordingly. We hoped to achieve this goal by a preliminary survey of the relationship of structural modifications to activity in our TNKS screening cascade and early in vitro ADME profiling. In addition to experimentally determined values, we relied on composite parameter analysis to help guide our hit-to-lead efforts.^{12–16}

We first examined the methyl and methoxy substituents on **3** (Table 1). Removal of the C-ring methyl group led to slightly increased potency in the biochemical assays but with a corresponding decrease in cellular activity. Replacing the methoxy with a methyl group on the B-ring (**4** vs **5**) resulted in a nearly 10-fold reduction in potency, and we predicted that replacing the C-ring methyl with a methoxy would likewise improve the potency. Gratifyingly, **6** was more potent than **4** and with a significant improvement in lipophilic efficiency (LipE). Further exploration of the B-ring revealed the methoxy group to be the most optimal of the analogues surveyed (compounds **7–10**) and that methyl substitution at R2 had little effect.

Our initial in vitro profiling revealed **3** to be a broad-based cytochrome P450 (CYP) inhibitor with IC₅₀s from 1 to 2 μM against CYPs 2C9, 2D6, and 3A4 (Table 2). Hypothesizing that the pyridyl moiety could be responsible for the CYP inhibition, we next explored other ring systems that might mitigate this liability (Table 2).¹⁷ Phenyl, 2-furanyl, and 2-thiophenyl replacements (compounds **11–15**) were all inactive against TNKS2. With the possibility that TNKS activity of **3** could be due to the pyridyl nitrogen acting as an H-bond acceptor, we considered that a 4-fluorophenyl group might also be an H-bond acceptor, however, **15** was also inactive against TNKS2. Despite the lack of TNKS activity, we tested **15** and found that it did not appreciably inhibit CYP activity in our assays. While this result is consistent with known CYP450 inhibitors, the contribution of substituents at R2 and R3 to CYP450 affinity can not be excluded.

Our examinations of the scaffold found similar results as Waalder et al. in that the triazole, oxadiazole, and the

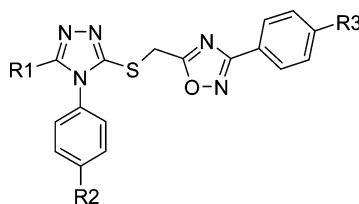
Table 1. Biochemical, Cellular, and LipE Values of B- and C-Ring Modifications of 3



compound	R1	R2	R3	IC ₅₀ (μM)			LipE ^a
				TNKS2	TNKS1	HEK293-STF	
3	OMe	H	Me	0.650	2.55	0.548	2.1
4	OMe	H	H	0.272	1.01	1.06	2.3
5	Me	H	H	1.88			1.0
6	OMe	H	OMe	0.175	0.559	0.341	3.2
7	OEt	H	OMe	0.509	1.761	0.919	2.2
8	Me	H	OMe	1.42			1.8
9	Me	Me	OMe	1.10			1.4
10	H	H	OMe	0.783			2.5

^aLipE = TNKS2 pIC₅₀ - cLogP.

Table 2. Biochemical and CYP SAR of Pyridyl Isoesters

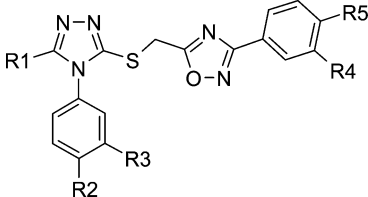


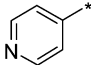
Compound	R1	R2	R3	IC ₅₀ (μM)			
				TNKS2	CYP 2C9	CYP 2D6	CYP 3A4
3		OMe	Me	0.650	0.99	1.2	1.7
11		OMe	Me	>19	-	-	-
12		H	H	>19	-	-	-
13		H	H	>19	-	-	-
14		H	H	>19	-	-	-
15		H	H	>19	>50	>50	>50

sulfanylmethyl linkage were all quite sensitive to modification with nearly all modifications examined having detrimental effects on activity (data not shown).¹¹ We therefore returned to the search of a pyridyl group replacement and were gratified to find **16** to be of equivalent potency and LipE as **3**, but with improved ligand efficiency (Table 3). Keeping R1 constant as methyl, we next surveyed B- and C-ring analogues. Whereas in the pyridyl series the addition of a meta methyl group on the B-ring very slightly enhanced potency (**8** vs **9**), a similar transformation on the methyl series (**16** vs **17**) resulted in a 4-fold decrease in potency with a more detrimental effect on composite parameters. The para fluorine analogue **18** had little

effect on potency but was held constant to examine C-ring analogues where **19** and **20** were found to be 4-fold more potent. Keeping the R5 modification with the highest LipE (**20**), we sought to further optimize the B-ring. As was seen in the pyridyl series, the 4-methyl substituent was suboptimal. Moving the methyl from the para to the meta position enhanced potency, LipE, and ligand efficiency (LE), which was intriguing in light of the previous comparison of **16** and **17**. Greater size at R2 was apparently not well tolerated, as **23** had a 4-fold decline in activity, but the isosteric methoxy group **24** resulted in double-digit nanomolar potency against TNKS2 with a substantial boost in LipE and LE. An additional R4

Table 3. SAR of 5-(5-Methyl-4-phenyl-4H-[1,2,4]triazol-3-ylsulfanylmethyl)-3-phenyl-[1,2,4]oxadiazole Analogues Including LipE and LE Analyses



Compound	R1	R2	R3	R4	R5	TNKS2		
						IC ₅₀ (μM)	LipE ^a	LE
3		OMe	H	H	Me	0.650	2.1	0.19
16	Me	Me	H	H	Me	0.589	2.1	0.23
17	Me	Me	Me	H	Me	2.04	1.1	0.20
18	Me	F	H	H	Me	1.07	2.2	0.22
19	Me	F	H	H	Cl	0.281	2.6	0.24
20	Me	F	H	H	OMe	0.197	3.4	0.24
21	Me	Me	H	H	OMe	0.629	2.5	0.22
22	Me	H	Me	H	OMe	0.132	3.2	0.25
23	Me	Et	H	H	OMe	2.63	1.4	0.19
24	Me	OMe	H	H	OMe	0.033	4.3	0.26
25	Me	OMe	H	OMe	OMe	0.042	4.5	0.24
26	Me	H	H	OMe	OMe	0.861	2.7	0.20

^aLipE = TNKS pIC₅₀ - cLogP.

Table 4. In Vitro Profile of Select Compounds Including Cellular Activity, CYP, hERG, and Microsomal Stability Data

compound	IC ₅₀ or EC ₅₀ (μM)							ER ^a	
	Axin2	STF	PARP1	PARP2	CYP2C9	CYP3A4	hERG	rat	human
1	0.371	0.078	1.18	0.134	>50	>50	>30	0.88	0.79
3	0.566	0.548	>19	>19	0.99	1.7	>30	0.96	0.95
24	0.709	0.215	>19	>19	21	5.7	>30	>0.97	0.97
25	0.375	0.126	>19	>19	45	5.3	>30	>0.97	0.97

^aExtraction ratio from liver microsomes.

methoxy group (compounds **25** and **26**) did not improve this series, but **26** confirmed the importance of the R2 methoxy analogue. Direct binding measurements of compound **24** against both TNKS1 and TNKS2 resulted in K_D values of 79 and 28 nM, respectively (Supporting Information Figure S1). Compound **24** was chosen for more extensive in vitro, structural, and early ADME profiling.

Both **24** and **25** demonstrate cellular PD effects as both stabilize Axin at a similar level as **3**, but with more potent Wnt pathway inhibition as measured by the HEK293-STF assay (Table 4). None of the compounds had any effect on luciferase activity in the HEK293-CRE assay, which is not dependent on Wnt signaling.⁴ The pyridyl moiety of **3** appears to be the main contributor to the DDI potential as **24** has no apparent CYP2D6 liability (IC₅₀ > 50 μM for **24** and **25**) and substantially reduced the CYP2C9 activity, however, some

CYP3A4 activity remained. This series appeared to be devoid of a significant signal in the hERG radioligand binding assay, however, we were cautious with this interpretation due to the low solubility of this series (typically <5 μM at pH 6.8, data not shown). The microsomal stability of this series was exceptionally low, with several likely metabolic soft spots including the electron-rich 4-methoxyphenyl moieties and sulfanylmethyl linker, all of which were required for effective TNKS inhibition. The low microsomal stability correlates well with the rapid in vivo clearance as **3** had a 15 min half-life in mice following iv dosing.¹¹ We confirmed that **3** and other analogues in this series are not inhibitors of PARP1 or PARP2 in our biochemical assays (Table 4), and the lack of structural similarity with typical PARP inhibitors suggested that this series might not bind as a nicotinamide mimetic.

Structural Studies. The crystal structure of the catalytic domain of human TNKS1 complexed with **24** was determined to 1.95 Å resolution. The final model was refined to an *R* factor of 17.2% (Table 5) and includes residues Gly1105–Arg1281

Table 5. Crystallographic Data and Refinement Information

parameters	TNKS1/24 complex
space group	C2
<i>a</i> , (Å)	124.3
<i>b</i> , (Å)	44.7
<i>c</i> , (Å)	88.2
α (deg)	90
γ (deg)	90
β (deg)	90.2
resolution range (Å)	44.10–1.95
total observations	119798
unique reflections	35563
completeness (%) ^a	99.5 (99.7)
<i>I</i> / σ ^a	15.2 (3.7)
<i>R</i> _{sym} ^{a,b}	0.054 (0.312)
<i>R</i> _{cryst} / <i>R</i> _{free} ^c	0.172/0.225
protein atoms	3342
heterogen atoms	440
solvent molecules	326
average <i>B</i> factor (Å ²)	25.9
rms Deviations from Ideal Values	
bond lengths (Å)	0.01
bond angle (deg)	1.02

^aNumbers in parentheses are for the highest resolution shell. ^b $R_{sym} = \sum |I_h - \langle I_h \rangle| / \sum I_h$ over all *h*, where *I_h* is the intensity of reflection *h*. ^c R_{cryst} and $R_{free} = \sum ||F_o| - |F_c|| / \sum |F_o|$, where *F_o* and *F_c* are observed and calculated amplitudes, respectively. *R_{free}* was calculated using 5% of data excluded from the refinement.

and Tyr1289–Ala1315 in molecule A, residues Gly1105–Glu1314 in molecule B, one zinc ion and one molecule of inhibitor **24** per protein molecule, six sulfate ions, four glycerol molecules, and 326 solvent molecules. The loop from Pro1282–Ala–1288 in molecule A and the 12 and 13 C-terminal residues of molecule A and B, respectively, were omitted from the final model because of poor electron density. The overall fold of the protein is very similar to the apo structure of TNKS1,¹⁸ with an overall 1.7 Å rms deviation for all C α atoms. However, substantial conformational flexibility is observed in the D-loop, residues Ala1202–Ala1210. As noted by Lehtio et al.,¹⁸ this change is essential to allow access to the enzyme's active site. In the apo structure, Tyr1203 lies across the NAD⁺ binding pocket making a hydrogen bond with the carbonyl oxygen of Tyr1224, blocking the substrate from binding. In the inhibited structure, we observe rearrangement of the Tyr1203 to point away from the active site, hence allowing the inhibitor access to the groove. The changes in this loop also effect the conformation of the loop containing Gln1262–His1270 between the β_6 and β_7 strands. This rearrangement is necessary to accommodate the new position of the D-loop in which Met1207 and Phe1208 bury themselves toward the protein core. This conformation adopted by the D-loop is very similar to the conformation seen in the inhibited TNKS2 structure.¹⁹ After removing these two loops, the overall rms deviation for C α atoms is lowered to 0.98 Å.

As seen in Figure 4, the inhibitor **24** is bound to the NAD⁺ donor site, as defined based on similarity with mono(ADP-

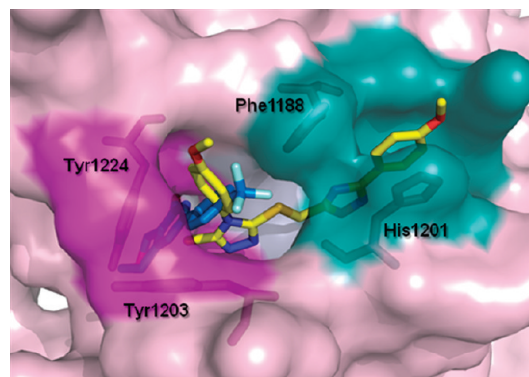


Figure 4. NAD⁺ binding pocket of TNKS1 with nicotinamide site in purple and adenosine site in green. Overlay of **1** (blue) in complex with TNKS2 and **24** (yellow) in complex with TNKS1. Among PARP family members, Phe1188 is unique to TNKS1/2, providing novel structural features for structure based drug design.

ribosyl)ating toxins.²⁰ The structure reveals that the inhibitor is bound to the adenosine/diphosphate linker portion of the NAD⁺ donor site with additional interactions in a hydrophobic nook which neighbors the diphosphate linker portion of the site. Strikingly, there are no interactions with the nicotinamide subsite as is seen with all PARP inhibitor complex structures to date, including **1** (Figure 4).^{21–24} Inhibitor **24** does not have the typical stacking interactions between Tyr1213 and Tyr1224 nor the hydrogen bonds with the amide of Gly1185 and side chain of Ser1221 that are typically seen with PARP inhibitors. The closest interaction with this portion of the pocket are van der Waals interactions between the 5-methyl of the triazole and the phenyl ring of Tyr1224. The side chain position of Tyr1224 has moved into the nicotinamide site to accommodate this interaction when compared to the apo structure, with a change of 2.4 Å at the tyrosine hydroxyl position. Additionally, the side chain of the catalytic Glu1291 has moved to make a hydrogen bond with the hydroxyl of Tyr1224, an interaction which is not seen in previous TNKS structures.

Key interactions between TNKS1 and inhibitor **24** can be seen in Figure 5, including two hydrogen bonds. The first is formed between the triazole nitrogen and the backbone amide of Tyr1213, and the second is formed between the oxadiazole nitrogen and the backbone amide of Asp1198. The methoxyphenyl oxadiazole binds into the adenosine portion of the binding groove. van der Waals interactions are seen with side chains of Phe1188, Ala1191, and Ile1192 on one side of the groove and a stacking interaction with the side chain of His1201 on the opposite side. When compared to the apo TNKS1 structure, the side chain of Phe1188 has moved ~1.5 Å away from the groove to accommodate the interaction, and there is a small change in the position of His1201 to optimize the stacking interaction. On the opposite side of the inhibitor, the methoxyphenyl triazole places the triazole above the nicotinamide site packed in between the C β of Tyr1203 and the side chain of His1184. The methoxyphenyl binds into a hydrophobic nook with the phenyl ring, making van der Waals interactions with C β of Ser1186, Pro1187, Phe1188, and Ile1228. One of the most interesting observations around this hydrophobic nook is that the phenyl ring of Tyr1203 in the TNKS1 apo structure exactly overlays with the phenyl ring of inhibitor **24**, hence inhibitor **24** may be taking advantage of a physiologically relevant subsite. Interactions in this area may contribute to the selectivity over PARP1/2, as this hydrophobic

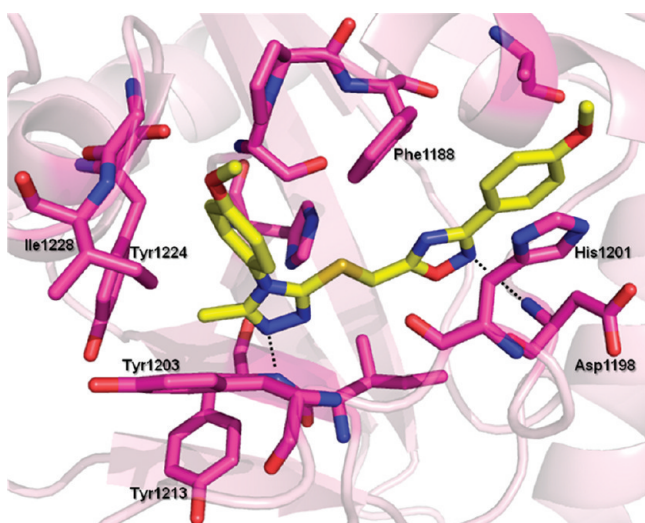


Figure 5. Crystal structures of **24** with TNKS1 showing NAD⁺ binding pocket residues and hydrogen bond interactions. TNKS provides two hydrogen bond donors for the adenosine pocket binder **24**.

nook is not conserved in the PARP family. Last, the sulfur atom in the linker of inhibitor **24** is also making a van der Waals interaction with the side chain of Phe1188, completing the inhibitor's C-shaped van der Waals interactions that wrap around Phe1188. Importantly, Phe1188 is also not conserved within the PARP family and probably has significant

contribution to the selectivity of this class of inhibitor for TNKS1/2 over PARP1/2. The amino acid of Phe1188 in TNKS1/2 corresponds to a nonaromatic residue in all other PARP family members, with the exception of PARP9 (tyrosine), suggesting selectivity versus other isoforms may be achievable by targeting this region.

To further quantify the binding site comparison between these two compounds, we calculated ligand-binding site residue contact areas for **1** and **24**. We calculated the amount of exposed surface area of residues proximate to each ligand that is in contact with the ligands (Figure 6) using ICM.²⁵ We hypothesize that despite the greater contact of **24** its "fit" to the binding site is less optimal than **1**, which prefers the nicotinamide site.

While the qualitative change in binding mode between **1** and **24** is clear, there are some notable changes in residues that are proximate to both ligands. For example, Phe1188 shows a large increase in contact area with **24** over **1** despite similar exposed areas for this residue. The side chain of Phe1188 has moved in such a way that it forms an edge to face interaction with the phenyl group of **24** that occupies the nook. The crystal structure of **24** therefore suggests that the plasticity of Phe1188 may permit access between the nicotinamide and adenosine pocket.

Docking Model Aids In Interpreting The SAR. A docking model was created using the receptor structure of **24** bound to TNKS1 using the ICM software to help understand the SAR further. The sequence of TNKS1 has identical residues in the binding site and 88% sequence identify overall with

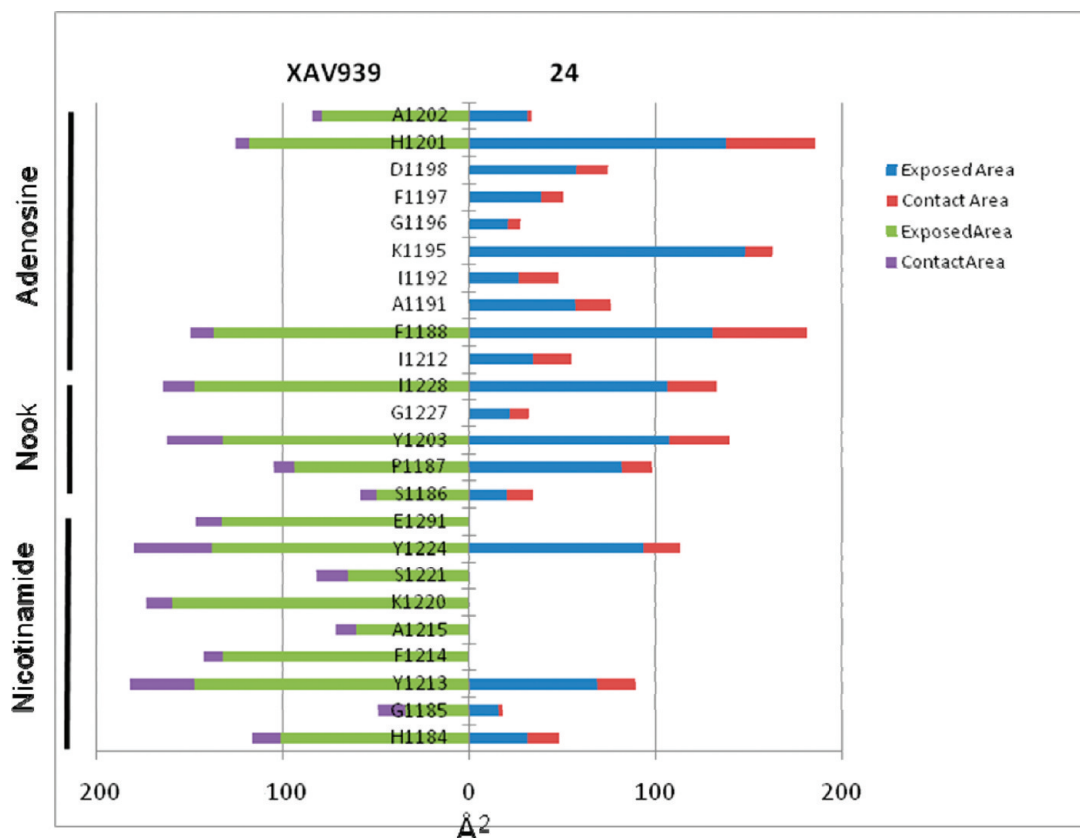


Figure 6. The amount of exposed surface area of residues proximate to the ligand that is in contact with the ligand in the binding site. Residue Y1203 is included in the nook definition as it can act to make contact with ligands that occupy the nook or fill the nook in the apo structure (pdb code 2RF5).

TNKS2. The docking model provided good correlation between the docking scores and the IC_{50} s (Figure 7), which

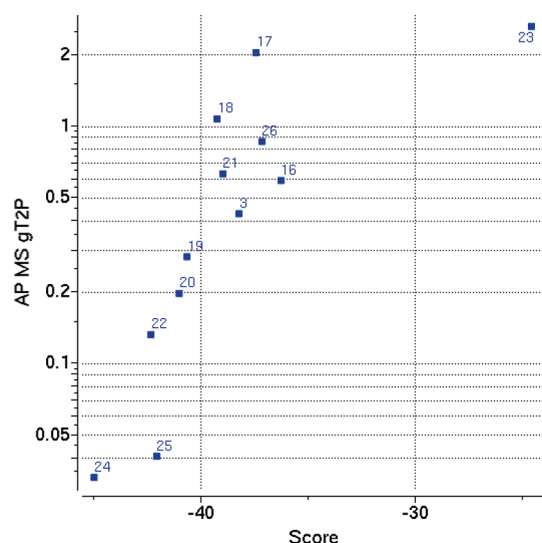


Figure 7. Comparison between calculated docking score and experimentally determined TNKS2 IC_{50} (μM) in log₁₀ scale.

allowed us some confidence in comparing and interpreting the binding modes (Figure 8) with the IC_{50} s. Much of the SAR of Table 3 can be explained from visual inspection of the computational results. The improved potency of **24** ($IC_{50} = 0.033 \mu M$) over **23** ($IC_{50} = 2.63 \mu M$) may be due to a more optimal fit to the nook region characterized by an enhanced electrostatic interaction between the O of the methoxy and the backbone N of Ile1228 in the nook region of the binding site and an edge-to-face aromatic interaction with Phe1187 that is enhanced with the methoxy over the ethyl group. Compound **3** ($IC_{50} = 0.650 \mu M$) has the methoxy in the nook region, but docking suggests that the pyridyl group is suboptimal for the nicotinamide region relative to the Me of **24** (Figure 8C). The

C-ring SAR is consistent with the solvent exposure of the meta position (R4 in Table 3). The fact that substituents at this position did not affect potency (compounds **25** and **26**) may be due to these modifications projecting into solvent rather than making any productive interactions with the TNKS protein.

CONCLUSION

We described here the characterization of a novel series of inhibitors of Wnt signaling that are potent and selective dual inhibitors of TNKS1/2 that are devoid of activity against PARP1 or PARP2. A preliminary survey of this series utilizing composite parameter analysis helped identify several analogues with low nanomolar TNKS inhibition and submicromolar activity in cellular models of Wnt pathway signaling and PD readouts. A crystal structure of the leading compound in this series (**24**) was determined and showed an unprecedented binding mode with a PARP family member. This novel binding mode within the adenosine binding pocket of TNKS1/2 may infer a degree of selectivity against other PARP family members. Further studies would be needed to determine if this may impart affinity to other NAD binding proteins. The SAR in this series was consistent with docking models and helped prioritize this series within the context of a lead optimization campaign. The results of these efforts will be published in due course.

EXPERIMENTAL SECTION

Compounds **3**–**26** were obtained from Chemical Diversity Research Institute, Moscow, Russia. The purity of all compounds was determined using high resolution HPLC/MS characterization and found to be >95% pure except as noted. High resolution LC/ESI-MS data were recorded using an Agilent 6220 mass spectrometer with electrospray ionization source and an Agilent 1200 liquid chromatograph with a gradient from 5% to 95% acetonitrile in water on a C18 reverse phase column with a diode array detection. The resolution of the MS system was approximately 11000 (fwhm definition). HPLC separation was performed using one of the methods (denoted in the header text) listed at end of report. Purine and hexakis(1*H*,1*H*,3*H*-tetrafluoropropoxy)phosphazine (protonated molecules *m/z*

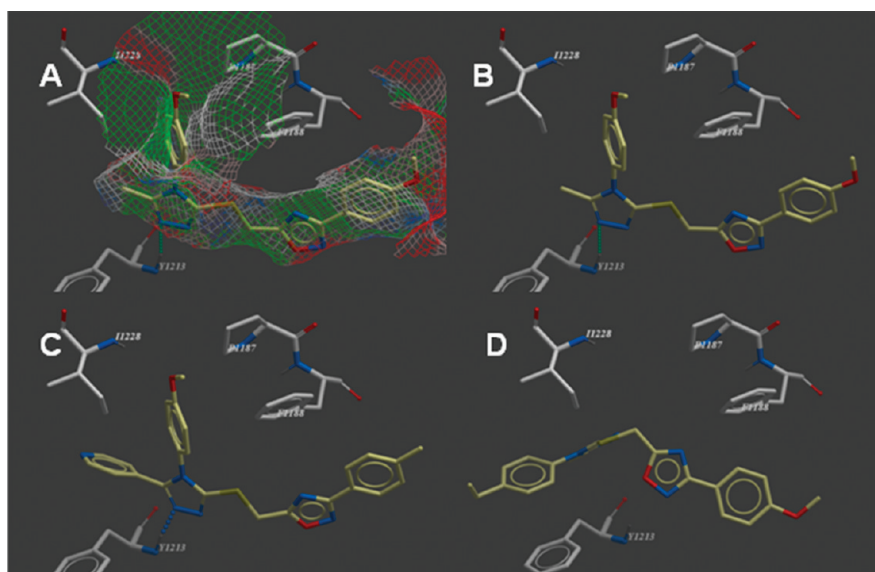


Figure 8. Binding poses for docking runs. (A) **24** docking pose with ligand surface colored by preferred ligand atoms (red, hydrogen bond acceptor; blue, hydrogen bond donor; green, hydrophobic; white, aromatic). (B) Docking pose of **24** without ligand surface. (C) Docking pose of **3** without ligand surface. (D) Docking pose of **23** without ligand surface.

121.05087 and 922.00979, respectively) were used as a reference. The mass accuracy of the system has been found to be <2 ppm.

Tankyrase AutoPARsylation Assay. PARP catalytic activity was monitored using the quantitative liquid chromatography/mass spectrometry (LC-MS) detection of nicotinamide, a product of the autoPARsylation reaction.

More specifically, the autoPARsylation reactions were performed at room temperature in 384-well Greiner flat-bottom plates (Costar, cat. no. 781201) using a final reaction volume of 40 μL and the following assay buffer conditions: 50 mM Tris-HCl, pH 7.5, 10 mM MgCl_2 , 50 mM NaCl, 250 μM NAD^+ , 1 mM DTT, 0.02% Tween-20, 8% glycerol.

The final reaction mixture contained 2.5% DMSO and inhibitors with concentrations ranging from 0.0086 to 18.75 μM . GST-TNKS2P, GST-TNKS1P, PARP1, and PARP2 enzymes were used at final concentrations of 20, 60, 5, and 2 nM, respectively. Following a 2 h incubation, the reaction mixtures were quenched by the addition of 10 μL of 20% formic acid containing 500 nM nicotinamide- d_4 (CDN Isotopes, Inc., cat. no. D3457). The protein was then precipitated by the addition of 2 volumes of acetonitrile followed by centrifugation (3000g, 20 min). The nicotinamide concentration in the resulting supernatants was measured by LC-MS.

The % inhibition was calculated as: $(\text{control} - \text{sample}) / (\text{control} - \text{background}) \times 100$. "Control" is the average value of eight wells without compound, and "background" is the average of eight wells mixed with 5 \times quenching solution measured prior to initiation of the reaction.

LC-MS Method. Reaction mixture supernatants were submitted to chromatographic separation on a Hypercarb column (2.1 mm \times 20 mm, 5 μm particle, Thermo Scientific Inc.). The chromatographic mobile phases were (A) 25 mM ammonium bicarbonate and (B) acetonitrile (0.1% ammonium hydroxide). Nicotinamide was eluted at 1 mL/min using a 5–95% B gradient over 0.8 min (Agilent 1200SL LC system, LEAP CTC HTC autosampler) and analyzed by multiple reaction monitoring (MRM) on a API4000 QTrap mass spectrometer (ABSciex, Framingham, MA) in the positive electrospray ionization (ESI+) mode. The mass transition for nicotinamide and nicotinamide- d_4 were 123 \rightarrow 80 and 127 \rightarrow 84, respectively. The relative responses (nicotinamide/nicotinamide- d_4) were measured at varied inhibitor concentrations and used to calculate inhibitory IC_{50} values (normalized IC_{50} regression curves, XLFit).

SuperTop Flash (STF) Reporter Gene Assay. Compound activity in inhibiting Wnt ligand-induced signaling was measured using a Wnt-responsive SuperTopFlash (STF) luciferase reporter gene assay in HEK293 cells. On day one of the assay, cells were plated at a density of 8000 cells per well of 384-well plate in 25 μL of medium containing 5% fetal bovine serum (FBS). On the second day, 20 μL of Wnt3A condition medium (CM) produced from mouse L cells were added to the cells to induce Wnt signaling, followed by addition of 5 μL of compounds to each well in 10-point serial dilution. On the third day, the luciferase activity was measured by the Bright-Glo Luciferase Assay System following manufacturer's protocol (Promega, E2620). The % Inhibition was calculated as: $(\text{maximum Wnt-induced signaling} - \text{sample}) / (\text{maximum Wnt-induced signaling} - \text{background}) \times 100$. "Maximum Wnt-induced signaling" is the STF signal level induced by 20% Wnt3A CM without compound; and "background" is the STF signal level without the addition of Wnt3A CM or compound. To demonstrate the specific activity of inhibitors regulating Wnt signaling, counterscreen was performed in HEK293T cells expressing a cAMP-response element (CRE) luciferase reporter gene. Compound activity on the CRE-reporter was measured in the presence of 10 μM Forskolin, which is an activator of cAMP signaling.

Axin2 Protein ELISA. Compound activity in stabilizing the Axin2 protein was measured by Sandwich enzyme-linked immunosorbent (ELISA) assay in the colorectal cell line SW480. Then 30000 SW480 cells were seeded per well in 96-well plate and incubated overnight prior to compound treatment. Cells were then treated with compounds in six-point dilution starting at 10 μM for 24 h. Cells were then washed with 100 μL of cold phosphate buffered saline (PBS) and lysed in 125 μL of cold 1 \times lysis buffer (Cell Signaling Technology, 9803) supplemented with protease inhibitor (Roche,

11836170) and phosphatase inhibitors (Sigma, P2850, P5726). For the ELISA assay, anti Axin-2 capture antibody was diluted to a concentration of 1 $\mu\text{g}/\text{mL}$ (1:1000) in carbonate coating buffer, pH 9.2 (Sigma, C3041–50CAP). Then 100 μL of the diluted anti Axin-2 capture antibody per well was used to coat the 96-well plate overnight at 4 $^\circ\text{C}$. Plates were then washed three times with wash solution, PBST20 (PBS + 0.05% Tween), and blocked with 1% BSA/PBS for 1.5 h at room temperature while shaking gently. After blocking, plates were then washed three times with wash solution. Then 100 μL of prepared SW480 cell lysate was added to each well and incubated at room temperature for 2 h while shaking gently. After washing, 100 μL of biotinylated anti-Axin2 antibody was added to each well and incubated at room temperature for 2 h. Signal was detected by chemiluminescence (Pierce SuperSignal ELISA Femto no. 3704) using streptavidin-HRP (R&D systems, DY998) and measured on PerkinElmer Wallac 1420 plate reader.

Crystallization. TNKS1 (1105–1327) plus an N-terminal cloning artifact of one glycine was purified²⁴ and concentrated to 10 mg/mL in 25 mM Tris pH 8.0, 200 mM NaCl, and 1 mM TCEP. Then 1 mM PJ34 was added to the protein prior to crystallization.²⁶ Crystals were grown using the hanging drop method where the protein was mixed 1:1 with a crystallization solution containing 100 mM bis-Tris pH 5.8, 15% PEG 3350, and 300 mM ammonium sulfate. The crystals were transferred to a solution containing 100 mM bis-Tris pH 5.8, 18% PEG 3350, 350 mM ammonium sulfate, and 0.2 mM compound **24**, and this solution was refreshed once per hour over a four-hour period. The crystals were then cryoprotected using same solution with the addition of 20% glycerol and flash frozen in liquid nitrogen.

Structure Determination. Diffraction data for the TNKS1/compound **24** complex were collected on a Dectris Pilatus 6 M detector at the Swiss Light Source beamline X06SA at a wavelength of 1 \AA . The data were measured from a single crystal, and the reflections were indexed, integrated, and scaled using XDS.²⁷ The space group of the complex was C2 with two molecules in the asymmetric unit. Structure was determined with Fourier methods using the program BUSTER,²⁸ the starting model was TNKS1/PJ34 structure (PDB code 3UH2) with ligand and active site waters removed.²⁴ Structure determination was achieved through iterative rounds of positional and simulated annealing refinement using BUSTER and model building using COOT.²⁹ Individual *B* factors were refined using an overall anisotropic *B* factor refinement along with bulk solvent correction. The solvent, sulfate ions, glycerol molecules, and compound **24** were built into the density in later rounds of the refinement. Data collection and refinement statistics are shown in Table 4.

Direct Binding Measurements. Direct binding measurements of inhibitor **24** to TNKS1 and TNKS2 were measured using a Biacore T100. Avi-tagged TNKS1 (1105–1327) and TNKS2 (950–1166), which were biotinylated with biotin ligase during expression, were immobilized on a streptavidin coated Biacore chip in HBS-N (10 mM HEPES, pH 7.4, 150 mM NaCl) and 0.25 mM TCEP at a flow rate of 10 $\mu\text{L}/\text{min}$ to levels of 3100 and 3300 RUs, respectively. Following immobilization, the assay buffer was modified to include surfactant 0.05% P-20 and 2% DMSO and the surface was allowed to stabilize using a flow rate of 50 $\mu\text{L}/\text{min}$. Inhibitor **24** was resuspended in running buffer and run at concentrations ranging from 1 μM to 1 nM through 2-fold dilutions. Data was fit using a 1:1 binding model in the Biacore T100 evaluation software version 2.0.1 (Biacore AB; Uppsala, Sweden).

ICM docking. We used chain A of crystal structure of **24** as the basis for model building and docking using the ICM modeling software.^{30–32} The receptor for docking was prepared in the following ways. First, we removed any water and counterions; only the protein and ligand structure remained. Second, we assigned atom types and bond orders for the protein and the ligand, hydrogen atoms, and force field parameters (MMFF) using an automated procedure in ICM.³⁰ Third, we optimized the hydrogens positions, including tautomeric states for ionizable residues, in their local environments using ICM.³⁰ Fourth, we removed the ligand **24** from the receptor and generated grid maps at 0.5 \AA for the binding site around the ligand. The grid dimensions were set to span the binding site from the nicotinamide to

adenosine pockets. Finally, the ligands to be docked were prepared for docking by the same automated procedure described above.

The ligands were docked into the grid maps of the receptor using the dockScan script in ICM.³⁰ A thoroughness value of 10 was used to ensure convergence of the biased Monte Carlo minimization docking method in ICM.²⁸ The top docking scored conformations for the ligands were rescored using the VLS scoring function in ICM, and the VLS score was used for the final ranking of ligands.³⁰ The final docking results scores for the ligands were compared against the binding IC₅₀ values (AUC of 0.83 for the ROC curve Supporting Information Figure S2)

■ ASSOCIATED CONTENT

● Supporting Information

Surface plasmon resonance (SPR) sensorgrams for binding of compound **24** to TNKS1/2 and TNKS2 and receiver operating characteristic curve for docking results are provided. This material is available free of charge via the Internet at <http://pubs.acs.org>.

Accession Codes

PDB code for the structure is 3UDD.

■ AUTHOR INFORMATION

Corresponding Author

*Phone: +1 (617) 871-7551. E-mail: michael.shultz@novartis.com.

Present Address

[†]Sanofi-Aventis, Cambridge, MA

Notes

The authors declare no competing financial interest.

■ ACKNOWLEDGMENTS

The TNKS1/24 data collection was performed on the X06SA beamline at the Swiss Light Source, Paul Scherrer Institut, Villigen, Switzerland.

■ REFERENCES

- (1) Schreiber, V.; Dantzer, F.; Ame, J. C.; de, M. G. Poly(ADP-ribose): novel functions for an old molecule. *Nature Rev. Mol. Cell Biol.* **2006**, *7*, 517–528.
- (2) Hsiao, S. J.; Smith, S. Tankyrase function at telomeres, spindle poles, and beyond. *Biochimie* **2008**, *90*, 83–92.
- (3) Seimiya, H. The telomeric PARP, tankyrases, as targets for cancer therapy. *Br. J. Cancer* **2006**, *94*, 341–345.
- (4) Huang, S. M.; Mishina, Y. M.; Liu, S.; Cheung, A.; Stegmeier, F.; Michaud, G. A.; Charlat, O.; Wielle, E.; Zhang, Y.; Wiessner, S.; Hild, M.; Shi, X.; Wilson, C. J.; Mickanin, C.; Myer, V.; Fazal, A.; Tomlinson, R.; Serluca, F.; Shao, W.; Cheng, H.; Shultz, M.; Rau, C.; Schirle, M.; Schlegl, J.; Ghidelli, S.; Fawell, S.; Lu, C.; Curtis, D.; Kirschner, M. W.; Lengauer, C.; Finan, P. M.; Tallarico, J. A.; Bouwmeester, T.; Porter, J. A.; Bauer, A.; Cong, F. Tankyrase inhibition stabilizes axin and antagonizes Wnt signalling. *Nature* **2009**, *461*, 614–620.
- (5) Fancy, S. P.; Harrington, E. P.; Yuen, T. J.; Silbereis, J. C.; Zhao, C.; Baranzini, S. E.; Bruce, C. C.; Otero, J. J.; Huang, E. J.; Nusse, R.; Franklin, R. J.; Rowitch, D. H. Axin2 as regulatory and therapeutic target in newborn brain injury and remyelination. *Nature Neurosci.* **2011**, *14*, 1009–1016.
- (6) Dodge, M. E.; Lum, L. Drugging the cancer stem cell compartment: lessons learned from the hedgehog and Wnt signal transduction pathways. *Annu. Rev. Pharmacol. Toxicol.* **2011**, *51*, 289–310.
- (7) Lu, J.; Ma, Z.; Hsieh, J. C.; Fan, C. W.; Chen, B.; Longgood, J. C.; Williams, N. S.; Amatruda, J. F.; Lum, L.; Chen, C. Structure–activity

relationship studies of small-molecule inhibitors of Wnt response. *Bioorg. Med. Chem. Lett.* **2009**, *19*, 3825–3827.

(8) Chen, B.; Dodge, M. E.; Tang, W.; Lu, J.; Ma, Z.; Fan, C. W.; Wei, S.; Hao, W.; Kilgore, J.; Williams, N. S.; Roth, M. G.; Amatruda, J. F.; Chen, C.; Lum, L. Small molecule-mediated disruption of Wnt-dependent signaling in tissue regeneration and cancer. *Nature Chem. Biol.* **2009**, *5*, 100–107.

(9) In our HEK293-CRE assay for cytotoxicity, IWR-1 is weakly active (IC₅₀ = 8.1 μM) and thus some off-target activity may lead to higher activity in the HEK-293 STF assay. XAV939 has no activity in the HEK-293 CRE assay at 50 μM.

(10) Rippmann, J. F.; Damm, K.; Schnapp, A. Functional characterization of the poly(ADP-ribose) polymerase activity of tankyrase 1, a potential regulator of telomere length. *J. Mol. Biol.* **2002**, *323*, 217–224.

(11) Waaler, J.; Machon, O.; von Kries, J. P.; Wilson, S. R.; Lundenes, E.; Wedlich, D.; Gradl, D.; Paulsen, J. E.; Machonova, O.; Dembinski, J. L.; Dinh, H.; Krauss, S. Novel synthetic antagonists of canonical Wnt signaling inhibit colorectal cancer cell growth. *Cancer Res.* **2011**, *71*, 197–205.

(12) Reitz, A. B.; Smith, G. R.; Tounge, B. A.; Reynolds, C. H. Hit triage using efficiency indices after screening of compound libraries in drug discovery. *Curr. Top. Med. Chem.* **2009**, *9*, 1718–1724.

(13) Abad-Zapatero, C.; Metz, J. T. Ligand efficiency indices as guideposts for drug discovery. *Drug Discovery Today* **2005**, *10*, 464–469.

(14) Hopkins, A. L.; Groom, C. R.; Alex, A. Ligand efficiency: a useful metric for lead selection. *Drug Discovery Today* **2004**, *9*, 430–431.

(15) Keseru, G. M.; Makara, G. M. The influence of lead discovery strategies on the properties of drug candidates. *Nature Rev. Drug Discovery* **2009**, *8*, 203–212.

(16) Leeson, P. D.; Springthorpe, B. The influence of drug-like concepts on decision-making in medicinal chemistry. *Nature Rev. Drug Discovery* **2007**, *6*, 881–890.

(17) Ortiz de Montellano, P. R. The 1994 Bernard B. Brodie Award Lecture. Structure, mechanism, and inhibition of cytochrome P450. *Drug Metab. Dispos.* **1995**, *23*, 1181–1187.

(18) Lehtio, L.; Collins, R.; van den Berg, S.; Johansson, A.; Dahlgren, L. G.; Hammarstrom, M.; Helleday, T.; Holmberg-Schiavone, L.; Karlberg, T.; Weigelt, J. Zinc binding catalytic domain of human tankyrase 1. *J. Mol. Biol.* **2008**, *379*, 136–145.

(19) Karlberg, T.; Markova, N.; Johansson, L.; Hammarstrom, M.; Schutz, P.; Weigelt, J.; Schuler, H. Structural basis for the interaction between tankyrase-2 and a potent Wnt-signaling inhibitor. *J. Med. Chem.* **2010**, *53*, 5352–5355.

(20) Ruf, A.; de, M. G.; Schulz, G. E. Inhibitor and NAD⁺ binding to poly(ADP-ribose) polymerase as derived from crystal structures and homology modeling. *Biochemistry* **1998**, *37*, 3893–3900.

(21) Hattori, K.; Kido, Y.; Yamamoto, H.; Ishida, J.; Kamijo, K.; Murano, K.; Ohkubo, M.; Kinoshita, T.; Iwashita, A.; Mihara, K.; Yamazaki, S.; Matsuoka, N.; Teramura, Y.; Miyake, H. Rational approaches to discovery of orally active and brain-penetrable quinazolinone inhibitors of poly(ADP-ribose)polymerase. *J. Med. Chem.* **2004**, *47*, 4151–4154.

(22) Kinoshita, T.; Nakanishi, I.; Warizaya, M.; Iwashita, A.; Kido, Y.; Hattori, K.; Fujii, T. Inhibitor-induced structural change of the active site of human poly(ADP-ribose) polymerase. *FEBS Lett.* **2004**, *556*, 43–46.

(23) Iwashita, A.; Hattori, K.; Yamamoto, H.; Ishida, J.; Kido, Y.; Kamijo, K.; Murano, K.; Miyake, H.; Kinoshita, T.; Warizaya, M.; Ohkubo, M.; Matsuoka, N.; Mutoh, S. Discovery of quinazolinone and quinoxaline derivatives as potent and selective poly(ADP-ribose) polymerase-1/2 inhibitors. *FEBS Lett.* **2005**, *579*, 1389–1393.

(24) Penning, T. D.; Zhu, G. D.; Gong, J.; Thomas, S.; Gandhi, V. B.; Liu, X.; Shi, Y.; Klinghofer, V.; Johnson, E. F.; Park, C. H.; Fry, E. H.; Donawho, C. K.; Frost, D. J.; Buchanan, F. G.; Bukofzer, G. T.; Rodriguez, L. E.; Bontcheva-Diaz, V.; Bouska, J. J.; Osterling, D. J.; Olson, A. M.; Marsh, K. C.; Luo, Y.; Giranda, V. L. Optimization of

phenyl-substituted benzimidazole carboxamide poly(ADP-ribose) polymerase inhibitors: identification of (*S*)-2-(2-fluoro-4-(pyrrolidin-2-yl)phenyl)-1*H*-benzimidazole-4-carboxamide (A-966492), a highly potent and efficacious inhibitor. *J. Med. Chem.* **2010**, *53*, 3142–3153.

(25) ICMref: Abagyan, R.; Orry, A.; Raush, E.; Budagyan, L.; Totrov, M. *ICM Manual 3.5*; Molsoft LLC: La Jolla, CA, 2007.

(26) Kirby, C.; Cheung, A.; Fazal, A.; Shultz, M.; Stams, T. Structure of Human Tankyrase-1 in Complex with Small Molecule Inhibitors PJ34 and XAV939. *Acta Crystallogr., Sect. F: Struct. Biol. Cryst. Commun.* **2012**, *F68*, 115–118.

(27) Kabsch, W. . XDS. *Acta Crystallogr., Sect. D: Biol. Crystallogr.* **2010**, *66*, 125–132.

(28) Afonine, P. V.; Grosse-Kunstleve, R. W.; Adams, P. D. A robust bulk-solvent correction and anisotropic scaling procedure. *Acta Crystallogr. D. Biol. Crystallogr.* **2005**, *61*, 850–855.

(29) Emsley, P.; Lohkamp, B.; Scott, W. G.; Cowtan, K. Features and development of Coot. *Acta Crystallogr., Sect. D: Biol. Crystallogr.* **2010**, *66*, 486–501.

(30) Totrov, M.; Abagyan, R. Flexible protein–ligand docking by global energy optimization in internal coordinates. *Proteins* **1997**, No. Suppl 1, 215–220.

(31) Abagyan, R.; Totrov, M. Biased probability Monte Carlo conformational searches and electrostatic calculations for peptides and proteins. *J. Mol. Biol.* **1994**, *235*, 983–1002.

(32) Abagyan, R.; Orry, A.; Raush, E.; Totrov, M. *ICM User Manual*; 2011; <http://www.molsoft.com/icm/>

(33) Lu, J.; Ma, Z.; Hsieh, J. C.; Fan, C. W.; Chen, B.; Longgood, J. C.; Williams, N. S.; Amatruda, J. F.; Lum, L.; Chen, C. Structure–activity relationship studies of small-molecule inhibitors of Wnt response. *Bioorg. Med. Chem. Lett.* **2009**, *19*, 3825–3827.